

Interfacial Solute Segregation in the Thermally Grown Oxide of Thermal Barrier Coating Structures

Yimeng Chen · Roger C. Reed ·
Emmanuelle A. Marquis

Received: 1 July 2014/Revised: 24 September 2014/Published online: 21 October 2014
© Springer Science+Business Media New York 2014

Abstract Atom probe tomography is used to measure interfacial and grain boundary segregation in the thermally grown oxide layers found on thermal barrier coatings formed by isothermal heat treatments at 1,100 °C. Segregation of Zr, Hf, Y, and minor elements at the metal/oxide interfaces, oxide grain boundaries and oxide dislocations are observed, quantified and rationalised. The implications of the findings are discussed.

Keywords Thermal barrier coating · Segregation · Atom probe tomography · Grain boundary · Dislocations

Introduction

For Ni-based superalloys to be used in very high temperature environments such as turbine blades, thermal barrier coatings (TBCs) are applied to shield the alloys from exceedingly high thermal exposures [1–4]. TBCs are multilayer structures made of a yttria-stabilized zirconia (YSZ) top coat with low thermal conductivity that is deposited on a so-called bond coat layer used to promote the adherence of YSZ with the alloy [5]. The bond coat layer is generally a Pt-modified β -aluminide layer or a Pt-modified γ/γ' layer [2]. During YSZ deposition and subsequent high temperature exposure, an Al_2O_3 layer (also called thermally grown oxide or TGO) forms and thickens between the bond coat and the YSZ top coat [6].

Y. Chen · E. A. Marquis (✉)
Department of Materials Science and Engineering, University of Michigan,
Ann Arbor, MI 48109-2136, USA
e-mail: emarq@umich.edu

R. C. Reed
Department of Materials, University of Oxford, Oxford OX1 3PH, UK

While TBCs can extend the life-time of the hottest components in turbine engines, they are prone to failure by a process associated with delamination away from the substrate [6, 7]. A large number of studies have been dedicated to elucidating the underlying mechanisms responsible for TBC failure and to the further improvement of TBCs with superior reliabilities at higher temperatures, e.g. [3, 5, 8, 9]. The delamination of TBCs from the substrate generally occurs at the TGO/bond coat interface, which can be attributed to the formation of interfacial cavities, segregation of detrimental impurities to interfaces, and residual stresses building up as the TGO thickens [7, 10, 11]. All of the factors above involve mass transport inside and between the components of the TBC structures. Adding trace amounts of reactive elements (REs)—e.g. La, Ce, Hf, Zr, Y—has been found to improve adhesion and also reduce the growth rate of TGO scales significantly [12]. The improved scale performance by adding REs has been mainly attributed to the segregation of REs to grain boundaries and scale/metal interfaces. Such segregation is thought to getter deleterious impurities such as sulfur [10] and/or to reduce the effective outward diffusivity of cations by blocking the available hopping sites or by modifying the interfacial structure/energy of the boundaries [13]. Previous transmission electron microscopy (TEM) observations and energy-dispersive X-ray spectroscopy (EDX) measurements have revealed the presence of Hf, Ta, Y, and Zr at grain boundaries in various TBC structures [14, 15]. More recently, atom probe tomography (APT) has been used successfully to study the chemistry of the TGO layer and the underlying alloy in an as-grown TBC structure showing Pt segregation at the alloy/TGO interface [16]. While the APT technique can in some instances exhibit a number of potential limitations that include peak overlaps, biased detection of multiple hits, or inaccurate three dimensional reconstructions, APT has the significant advantage of providing quantitative solute measurements, thereby complementing qualitative EDS mapping and resolving potential EDS peak overlaps that are different than those observed in the APT mass spectra. To complement the existing qualitative TEM data on RE segregation to grain boundaries, this work reports on the quantitative analyses of grain boundary and interfacial chemistry in the thermally grown layers of oxidized TBC structures.

Experimental Methods

Two TBCs were used to investigate the chemistry of grain boundaries and dislocations in the TGO layers (alumina). These TBCs were grown on two single-crystal alloys with slight differences in compositions; these are listed in Table 1. The procedures of TBC coating for samples A and B were identical. The alloys were grit-blasted to roughen the surface before deposition of a 10–12 μm thick Pt layer. A heat treatment at 1,100 $^{\circ}\text{C}$ for 1–4 h was used to allow Pt to diffuse into the substrate thereby forming the bond coat layer. Finally, an yttria-stabilised zirconia (ZrO_2 -7 wt% Y_2O_3) top coat layer with a thickness of $\sim 100 \mu\text{m}$ was deposited at 1,150 $^{\circ}\text{C}$ by electron beam physical vapor deposition (EB-PVD). The TGO layers formed between top coat and bond coat were thickened by iso-thermal aging at 1100 $^{\circ}\text{C}$ in air for 3 h (sample A) and 250 h (sample B).

Table 1 Compositions (in at. %) of alloys A and B. The nominal values are before Pt deposition and taken from [9, 34] for alloy A and [34] for alloy B. The γ and γ' compositions in the alloys and bond coats were measured by APT

	Ni	Pt	Co	Cr	Mo	W	Re	Al	Ta	Hf	Fe	Ti	Si	Nb	C
Alloy A (nominal)	bal.	–	10.0	7.6	0.4	2.1	1.0	12.7	2.2	0.03	–	–	–	–	–
Alloy B (nominal)	bal.	–	2.1	4.8	1.4	1.8	1.6	13.3	2.6	0.03	–	–	–	–	–
γ' in alloy A	bal.	–	6.3	2.2	0.3	1.5	0.2	16.3	3.0	0.02	0.03	1.55	0.11	0.01	0.01
γ in alloy A	bal.	–	20.4	22.3	0.8	2.2	3.5	3.2	0.2	0.00	0.12	0.10	0.09	0.00	0.02
γ' in bond coat (A)	bal.	22.1	6.1	9.0	0.2	0.4	0.1	17.5	0.0	0.01	0.45	1.13	0.10	–	0.00
γ in bond coat (A)	bal.	18.8	10.2	14.6	0.5	1.3	0.6	8.0	0.4	0.00	0.66	0.39	0.16	–	0.01

APT specimens were prepared from the TGO scales by a standard lift-out method [17] and annular ion beam milling using a FEI Quanta 3D FEG microscope which allows scanning electron microscopy (SEM) observations during focused ion beam (FIB) milling [18]. APT specimens from sample A were prepared at different locations: in the original alloy to check for the presence of minor alloying elements and impurities, in the TGO layer near the bond coat interface, and at the interface between the TGO and the bond coat. The APT specimens from sample B were all prepared from the middle of the TGO layer. APT analyses were carried out using a CAMECA LEAP-4000X HR instrument operated in laser mode with a laser energy of 70–80 pJ per pulse. Specimens were maintained at a constant temperature of 50 K for sample A and 25 K for sample B. The detection rate was set to 0.005 atom per pulse for data acquisition. The raw data was reconstructed using the IVAS 3.6.4 software from CAMECA. The field factor was set at 3.3, while the image compression factor (ICF) and the evaporation field were varied so that the reconstructed data would show flat grain boundaries and straight dislocations. Typical values were 1.9 for the ICF and 35 V/nm for the evaporation field.

Thin foil TEM specimens from alloy A were also prepared by a lift-out and FIB milling approach [17]. The microstructure of the TGO/bond coat interface was observed by scanning transmission electron microscopy (STEM) using a JEOL 2010F TEM microscope operated at 200 kV. Energy dispersive X-ray spectroscopy (EDS) was used to estimate local compositions.

Results

TGO/Bond Coat Interface and TGO Grain Boundary Segregation (Sample A)

The cross-sectional microstructure of the TBC coating formed on sample A is shown in Fig. 1 with, from top to bottom, the YSZ top coat, regions of mixed phases and nanocrystalline grains, the thermally grown oxide, and the bond coat. The top coat has a columnar grain structure with some porosity evident near the bottom interface and in between grains. The nanocrystalline region has previously been identified as a mix of phases that include YSZ, Al_2O_3 , Cr_2O_3 , Pt and Ni metal particles [16, 19]. The thermally grown Al_2O_3 layer, which is only $\sim 1 \mu\text{m}$ thick, presents relatively large grains with grain boundaries running from the bond coat to the top coat or the nanocrystalline layer. The bond coat is expected to be the γ' phase. However, few isolated γ phase regions, identified by their higher Co and Cr and low Al concentrations, are observed along the TGO/bond coat interface as highlighted by the red solid lines in Fig. 1.

The metal/oxide interface was further characterized using APT and a representative dataset containing the interface and a TGO grain boundary is shown in Fig. 2. In the bond coat region under the TGO layer, both γ' and γ phases (identified by their compositional differences) are observed, in agreement with the TEM observations. The measured compositions are listed in Table 1 and reveal the presence of minor alloying elements, in particular Si and Ti. Zr and Y were not detected however. The measured composition of the TGO grains (away from grain

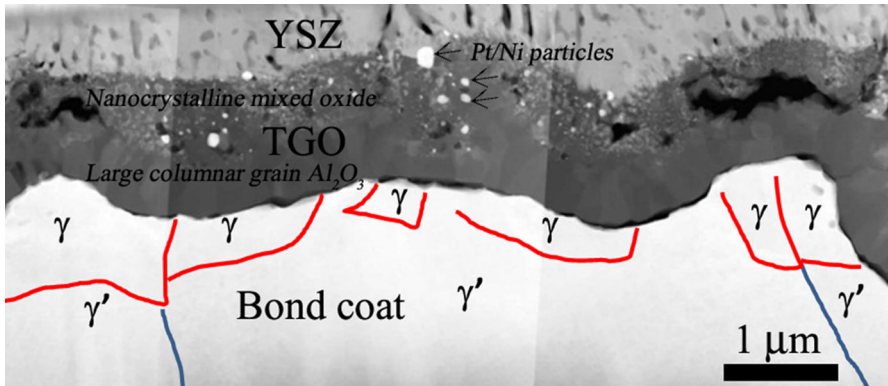


Fig. 1 Cross-sectional STEM image of the TBC structure in alloy A after oxidation at 1,100 °C for 3 h

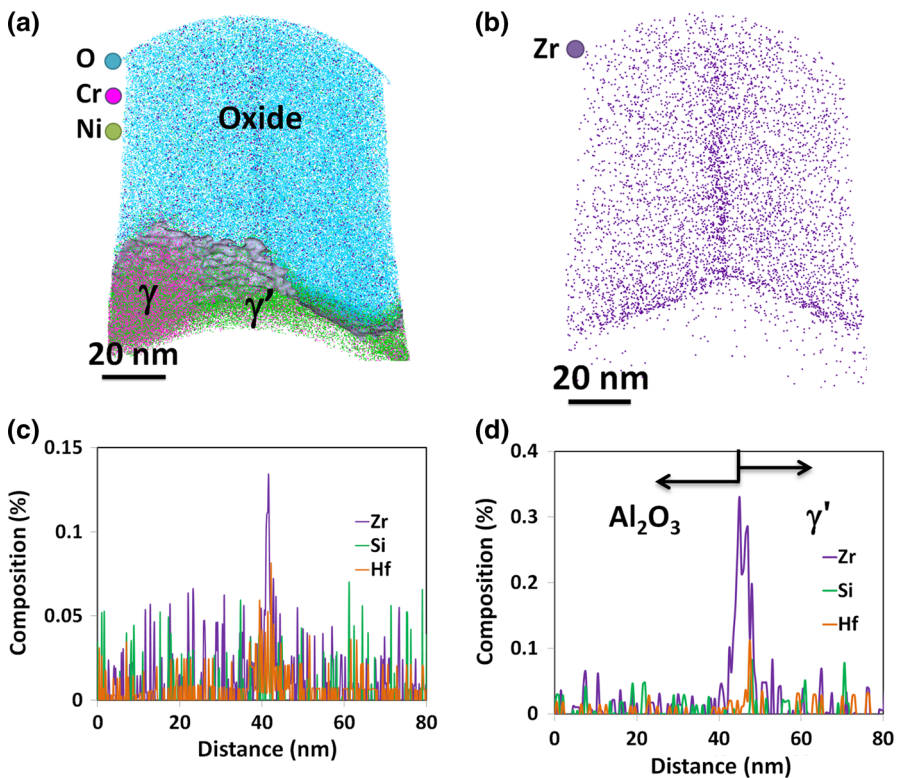


Fig. 2 Analysis of the TGO/bond coat interface. **a** APT reconstruction from sample A containing a TGO grain boundary and the TGO/bond coat interface. **b** the same volume showing Zr only. **c** One-dimensional concentration profile taken perpendicular to the TGO grain boundary shown in (a). **d** One-dimensional concentration profile taken perpendicular to the TGO/ γ' interface

Table 2 Gibbsian excess values (atom/nm²) for Zr, Hf and Si measured from six oxide grain boundaries. GB1 corresponds to the oxide grain boundary shown in Fig. 2

	GB1	GB2	GB3	GB4	GB5	GB6
Zr	0.10	0.09	0.10	0.12	0.10	0.06
Hf	0.05	0.05	0.05	0.05	0.06	0.08
Si	0.02	0.06	0.06	0.05	0.05	0.04
Total	0.17	0.20	0.21	0.22	0.21	0.19

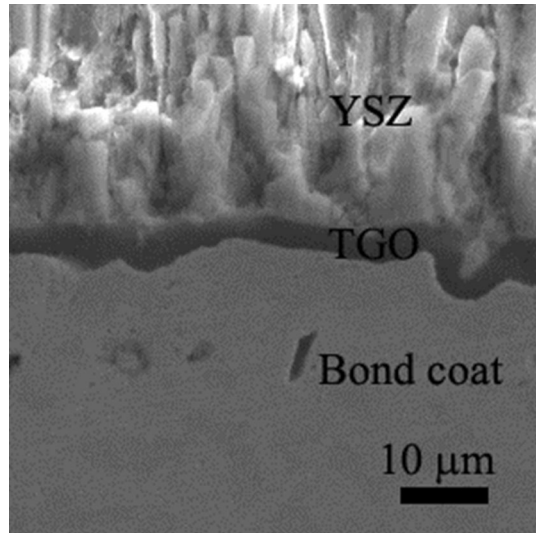
boundaries) is 43.0 ± 3.2 at.% Al and 57.0 ± 3.2 at.% O, which is typical for APT analyses of Al₂O₃ that systematically show an apparent sub-stoichiometry [20]. No other solute element was detected in Al₂O₃ above the background level, which for this particular dataset is estimated at 40 ppm around the mass-to-charge ratio (m/c) of 52.5 (YO²⁺). The distribution of Zr is shown separately in Fig. 2b and the Zr map is tilted for clarity to show the distribution of Zr at both the oxide grain boundary and the metal oxide interface. Note that the apparent presence of Zr within the TGO grains in Fig. 2b corresponds to noise rather than real Zr atoms. Alternatively, the higher density of Zr along a planar feature is indicative of a grain boundary with Zr segregation. Figure 2c is a one-dimensional concentration profile taken perpendicular to the oxide grain boundary in Fig. 2a. In addition to Zr, Hf and Si are also segregated to this boundary. A total of six different oxide grain boundaries were analyzed. Solute segregation was quantified using Gibbsian interfacial excess measurements [21] and the measured amounts are listed in Table 2. The cumulative excess for all solute elements is similar for all grain boundaries with an average value of 0.2 ± 0.02 atom/nm². For reference, this would correspond to ~ 15 % of a monolayer coverage of the basal plane of Al₂O₃. Some variations are observed from one boundary to another. The segregation levels for all segregating elements and particularly Si are smaller at GB1 than at the other grain boundaries. For GB6, the Hf content is higher than that of Zr. The possible segregation of other solute atoms, such as Y and C, was carefully checked but no segregation beyond the detectable limit could be confirmed.

At the TGO/bond coat interface, Zr segregation is revealed with a one-dimensional concentration profile taken perpendicular to the interface between the TGO and γ' phase (Fig. 2d). While not shown here, the observed segregation level at the oxide and γ interface is comparable. The interface analysis from three separate datasets provides an average Gibbsian excess of 0.4 ± 0.1 atom/nm², which is two times higher than the segregation at the TGO grain boundaries. No Hf was detected at the interface. However, the peaks of HfO overlap with Pt in the bond coat, thus reducing the detection limit of Hf at this interface.

TGO Grain Boundary and Dislocation Segregation (Sample B)

The oxidation of sample B at 1,100 °C for 250 h resulted in the formation of a thicker TGO layer (~ 3.5 μm thick) as shown in Fig. 3. Despite the prolonged oxidation, the interfacial integrity was maintained and no cracking was observed by

Fig. 3 Cross-sectional SEM image of the TBC structure in alloy B after oxidation at 1,100 °C for 250 h



SEM. However, APT analyses of the TGO/bond coat interface could not be obtained due to the systematic fracture of this oxide/metal interface during field evaporation of the specimens. Instead, APT samples were prepared from the center of the TGO layer. These specimens allowed the investigation of grain boundary segregation in the oxide phase. A representative analysis is shown in Fig. 4, revealing solute segregation at a grain boundary and along dislocations. Hf, Zr, Si, Y with small amount of C and Ti are segregated to the grain boundary (Fig. 4b), while dislocations (Fig. 4c) are enriched in Hf, Zr, Si and Y. The cumulative solute excess at the grain boundary is 1.57 atom/nm^2 , which would correspond to over 1 monolayer coverage on the basal plane of Al_2O_3 . The individual solute Gibbsian excesses are 0.56 Zr, 0.45 Hf, 0.28 Si, 0.22 Y, 0.03 C and 0.03 Ti atom/nm^2 . Solute excesses at the dislocations were measured by placing 9 nm diameter, 60 nm long cylinders centered on the dislocations seen in Fig. 4a. This diameter is larger than the apparent dislocation segregation width so as to include all segregated atoms. A background subtraction was then applied to the mass spectra to remove the matrix contribution. The average segregation excesses are 1.4 ± 0.5 Zr, 1.1 ± 0.5 Hf, 0.6 ± 0.1 Si, and 0.2 ± 0.1 Y atom/nm . The errors correspond to the standard deviations from the three visible dislocations. While the alloy substrate contains 2.6 at.% Ta, no Ta was observed in the TGO in any of the APT analyses performed in this work. On the other hand, Zr and Y were not detected in the bond coat. Since Co has been reported to affect the performance of TBC lifetimes [9], the possible presence of Co in the TGO was specifically checked for this sample. Although the mass to charge ratio at $^{59}\text{Co}^{+2}$ overlaps with AlO_2^+ from the field evaporation of Al_2O_3 , because of the absence of Co^{2+} and of any molecular cobalt oxide ions in the mass spectrum, it can be concluded that Co is not in the TGO layer.

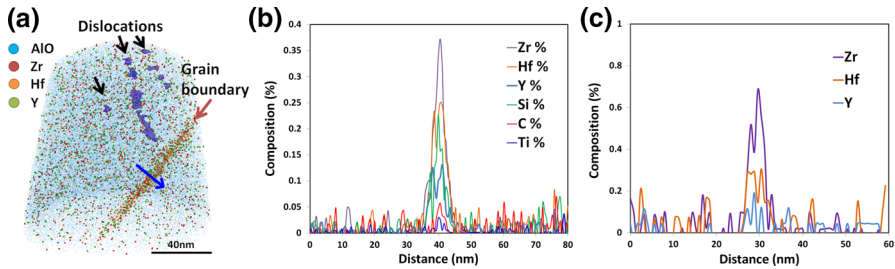


Fig. 4 **a** Ion distribution map from the Al₂O₃ scale illustrating solute segregations at a grain boundary and dislocations. **b** Concentration profile across the grain boundary in **(a)** along the blue arrow. **c** Zr and Hf concentration profile taken across one of the dislocations. Note that a 3 nm thick plate-shape region of interest was placed on one of the dislocations in **(a)** to generate the concentration profile. The thickness of the plate is comparable to the diameter of the line dislocations based on the 3D solute distribution (Color figure online)

Discussion

The generally beneficial effects of REs on the mechanical properties of Al₂O₃ and on limiting the growth of the alumina scale are well known. These two effects have been linked to REs segregation to the alumina grain boundaries. Indeed, it has been observed that RE segregation to bulk alumina grain boundaries is linked to improved creep strength [22] and RE-doped alumina scales have a lower creep rate than undoped scales [23]. It is also believed that the presence of REs at grain boundaries blocks or hinders the diffusion of oxygen or aluminum along grain boundaries [24]. While there are numerous observations of RE element segregation at Al₂O₃ grain boundaries, the relationships between segregation levels and oxide growth kinetics have never been quantitatively established. This work represents a first step towards the quantification of oxide grain boundary segregation using APT.

The two TBCs chosen in this work have identical top coats while the bond coats have slight differences in composition. The APT reconstructions of sample A were obtained from regions in the TGO layer immediately above the bond coat; these were 1.0 μm below the top coat. The APT reconstructions of sample B were obtained from the middle of the TGO layer that was ~1.7 μm below the top coat for the sample B. While Zr, Hf and Si were found segregating to TGO grain boundaries in both samples, Y segregation was only observed in Sample B. Due to the absence of Zr and Y in the bond coat, it is conceivable that their presences at grain boundaries must result from incorporation into the initial Al₂O₃ growth during the deposition of the top coat (7 wt% Y₂O₃–ZrO₂) and subsequent diffusion. The cumulative excess at grain boundaries increased by a factor of ~7 from Sample A to Sample B, correlating with the extended high temperature exposure. However, the absence of Y at the oxide grain boundaries in Sample A may also result from a sampling issue, whereby Y tends to cluster into particles rather than to segregate homogeneously along grain boundaries, as suggested by recent observations and calculations [25, 26]. The same calculations indicated that Hf atoms are less likely to form clusters resulting in a higher mobility along α-Al₂O₃ grain boundaries, which is consistent with the higher segregation levels.

The substrates contain nominally 0.03 at.% Hf, in common with many nickel-based superalloys, and confirmed by the APT compositional analysis of the γ' and γ phase in the bulk alloy (Table 1). The top coat composition was not analyzed but the original target used for deposition likely contained some amount of Hf since commercial grade zirconium typically contains from 1 to 3 at.% Hf [27]. The presence of Hf on scale grain boundaries may be a combined effect of inward diffusion from the top coat and initial incorporation in the TGO scale during top coat deposition. Zr most likely comes from the top coat as well. The exact mechanism of incorporation of Zr into the TGO layer is unclear, however mixing of Al_2O_3 and ZrO_2 can occur during the early stages of deposition [28]. Even though Ta is present in the original alloys and was previously reported to segregate at TGO grain boundaries [8], it was not detected in this work. Finally, the segregation of Si at the TGO grain boundaries is rationalized from its presence in the original alloy and the bond coat and by upward diffusion along the Al_2O_3 grain boundaries. A similar explanation may be provided for Ti in Alloy B although the composition of the bond coat was not measured.

In the case of sample A, small variations are observed from one grain boundary to another; the explanation may be thermodynamics or kinetics. Local chemistry variations and variations in grain boundary orientation and therefore grain boundary structure may lead to different segregation enthalpies. Such preferential segregation has been qualitatively reported for Si and Ti at different alumina bicrystals using HRTEM and EDX techniques [29], with enhanced segregation of Si and Ti at large angle random grain boundaries compared to low-angle grain boundaries. Similarly, Bouchet et al. reported that the levels of Y and Si segregation at Al_2O_3 grain boundaries also depend on grain boundary orientation with different dependence for each solute element [30]. Grain boundary structures could also affect the upward diffusion of the minor elements leading to variations in the observed segregation levels from one boundary to another. However due to the limited number of observations and the dynamic nature of the alumina coatings, the diffusion kinetics are beyond the scope of this article and will require further investigation. Note that the segregation levels measured here are much smaller than the expected saturation equilibrium levels for doped Al_2O_3 reported in [31].

Finally, the presence of dislocations in the TGO layer is not surprising. Grain boundary dislocations in oxide scales [32] and Ti, Y and Zr segregation to dislocations emitted from grain boundaries in the alumina scale formed on a FeCrAlY alloy [33] were previously observed using TEM. The different segregation levels between grain boundaries and dislocations suggest that the tetravalent elements such as Hf, Zr and Si segregate more to dislocations compared with the trivalent Y. Previous work however, reported that Y atoms strongly segregates to dislocations in Y-doped Al_2O_3 [30]. Therefore similar to grain boundaries, whether different dislocation structures and co-segregation effects may lead to different segregation behaviors would need clarification.

Conclusions

APT analyses were performed successfully to quantify solute segregation at grain boundaries and interfaces in the thermally grown oxide layers of TBCs. After only a

relatively short oxidation time, segregation of Zr, Hf, and Si is already present along TGO grain boundaries. Some variations in solute concentrations were observed for different boundaries. Zr was the most prevailing segregating element for most of the grain boundaries, with some boundaries richer in Hf. At the oxide/bond coat interface, Zr is the only segregated element. For longer oxidation times, additional Y, C and Ti segregation is observed at TGO grain boundaries. In addition, grain boundary dislocations in TGO also revealed Zr, Hf, and Si segregation.

Acknowledgments This work was partly supported by The University of Michigan College of Engineering.

References

1. D. V. Rigney, et al., PVD thermal barrier coating applications and process development for aircraft engines. *J Thermal Spray Technol* **6**, (2), 167–175 (1997).
2. R. C. Reed, *The superalloys: fundamentals and applications*, Cambridge University Press, Cambridge, (2006).
3. R. A. Miller, Current status of thermal barrier coatings—an overview. *Surf Coat Technol* **30**, (1), 1–11 (1987).
4. N. P. Padture, M. Gell and E. H. Ordan, Thermal barrier coatings for gas-turbine engine applications. *Science* **296**, 280–284 (2002).
5. M. Stiger, et al., Thermal barrier coatings for the 21st century. *Zeitschrift für Metallkunde* **90**, (12), 1069–1078 (1999).
6. A. Rabiei and A. Evans, Failure mechanisms associated with the thermally grown oxide in plasma-sprayed thermal barrier coatings. *Acta Mater* **48**, (15), 3963–3976 (2000).
7. M. Gell, et al., Mechanism of spallation in platinum aluminide/electron beam physical vapor-deposited thermal barrier coatings. *Metall Mater Trans A* **30**, (2), 427–435 (1999).
8. B. Pint, et al., Substrate and bond coat compositions: factors affecting alumina scale adhesion. *Mater Sci Eng A* **245**, (2), 201–211 (1998).
9. R. T. Wu, et al., The retention of thermal barrier coating systems on single-crystal superalloys: effects of substrate composition. *Acta Mater* **56**, (14), 3622–3629 (2008).
10. J. L. Smialek, Effect of sulfur removal on Al₂O₃ scale adhesion. *Metall Trans A* **22**, (3), 739–752 (1991).
11. A. G. Evans, et al., Mechanisms controlling the durability of thermal barrier coatings. *Progress Mater Sci* **46**, (5), 505–553 (2001).
12. D. Whittle and J. Stringer, Improvements in high temperature oxidation resistance by additions of reactive elements or oxide dispersions. *Philos Trans R Soc London Ser A* **295**, (1413), 309–329 (1980).
13. A. H. Heuer, et al., Alumina scale formation: a New Perspective. *J Am Ceram Soc* **94**, S146–S153 (2011).
14. B. Pint and K. More, Characterization of alumina interfaces in TBC systems. *J Mater Sci* **44**, (7), 1676–1686 (2009).
15. K. A. Unocic, C. M. Parish and B. A. Pint, Characterization of the alumina scale formed on coated and uncoated doped superalloys. *Surf Coat Technol* **206**, (7), 1522–1528 (2011).
16. Y. Chen, R. C. Reed and E. A. Marquis, As-coated thermal barrier coating: structure and chemistry. *Scr Mater* **67**, (9), 779–782 (2012).
17. L. A. Giannuzzi and F. A. Stevie, A review of focused ion beam milling techniques for TEM specimen preparation. *Micron* **30**, (3), 197–204 (1999).
18. K. Thompson, et al., In situ site-specific specimen preparation for atom probe tomography. *Ultra-microscopy* **107**, (2–3), 131–139 (2007).
19. K. S. Murphy, K. L. More and M. J. Lance, As-deposited mixed zone in thermally grown oxide beneath a thermal barrier coating. *Surf Coat Technol* **146–147**, 152–161 (2001).
20. E. A. Marquis, et al., Probing the improbable: imaging C atoms in alumina. *Mater Today* **13**, (10), 34–36 (2010).

21. O. C. Hellman, et al., Application software for data analysis for three-dimensional atom probe microscopy. *Mater Sci Eng A* **327**, 29–33 (2002).
22. J. Cho, et al., Role of segregating dopants on the improved creep resistance of aluminum oxide. *Acta Mater* **47**, (5), 4197–4207 (1999).
23. B. Veal and A. Paulikas, Growth strains and creep in thermally grown alumina: oxide growth mechanisms. *J Appl Phys* **104**, (9), 093525 (2008).
24. B. A. Pint, Experimental observations in support of the dynamic-segregation theory to explain the reactive-element effect. *Oxid Met* **45**, (1–2), 1–37 (1996).
25. S. Lartigue-Korinek, et al., HAADF study of the relationship between intergranular defect structure and yttrium segregation in an alumina grain boundary. *Acta Mater* **59**, (9), 3519–3527 (2011).
26. I. Milas, B. Hinnemann and E. A. Carter, Structure of and ion segregation to an alumina grain boundary: implications for growth and creep. *J Mater Res* **23**, (5), 1494–1508 (2008).
27. M. Sillassen, et al., Effects of dopant concentration and impurities on the conductivity of magnetron-sputtered nanocrystalline yttria-stabilized zirconia. *Solid State Ionics* **181**, (19), 864–867 (2010).
28. M. J. Stiger, et al., Development of intermixed zones of alumina/Zirconia in thermal barrier coating systems. *Metall Mater Trans A* **38A**, (4), 848–857 (2007).
29. M. Chi and H. Gu, Comparison of segregation behaviors for special and general boundaries in polycrystalline Al_2O_3 with SiO_2 – TiO_2 impurities. *Interface Sci* **12**, (2–3), 335–342 (2004).
30. D. Bouchet, F. Dupau and S. Lartigue-Korinek, Structure and chemistry of grain boundaries in yttria doped aluminas. *Microsc Microanal Microstruct* **4**, (6), 561–573 (1993).
31. M. Gülgün, et al., Cation segregation in an oxide ceramic with low solubility: yttrium doped α -alumina. *Interface Sci* **10**, (1), 99–110 (2002).
32. A. Heuer, N. J. Tighe and R. Cannon, Plastic deformation of fine-grained alumina (Al_2O_3): II, basal slip and nonaccommodated grain-boundary sliding. *J Am Ceram Soc* **63**, (1–2), 53–58 (1980).
33. A. Heuer, et al., On the growth of Al_2O_3 scales. *Acta Mater* **61**, (18), 6670–6683 (2013).
34. R. T. Wu and R. C. Reed, On the compatibility of single crystal superalloys with a thermal barrier coating system. *Acta Mater* **56**, (3), 313–323 (2008).